Classification Method to Define Synchronization Capability Limits of Line-Start Permanent-Magnet Motor Using Mesh-Based Magnetic Equivalent Circuit Computation Results

Bart Wymeersch [1,*] , **Frederik De Belie [1,2]** , **Claus B. Rasmussen [3]** and **Lieven Vandevelde [1,2]**

[1] Department of Electrical Energy, Metals, Mechanical Constructions and Systems (EEMMeCS), Ghent University, 9052 Zwijnaarde, Belgium; frederik.debelie@ugent.be (F.D.B.); lieven.vandevelde@ugent.be (L.V.)
[2] Flanders Make, 8500 Kortrijk, Belgium
[3] Department of Motor Engineering, Grundfos A/S, 8850 Bjerringbro, Denmark; cbrasmussen@grundfos.com
[*] Correspondence: bartj.wymeersch@ugent.be; Tel.: +32-9-264-57-03

Abstract: Line start permanent magnet synchronous motors (LS-PMSM) are energy-efficient synchronous motors that can start asynchronously due to a squirrel cage in the rotor. The drawback, however, with this motor type is the chance of failure to synchronize after start-up. To identify the problem, and the stable operation limits, the synchronization at various parameter combinations is investigated. For accurate knowledge of the operation limits to assure synchronization with the utility grid, an accurate classification of parameter combinations is needed. As for this, many simulations have to be executed, a rapid evaluation method is indispensable. To simulate the dynamic behavior in the time domain, several modeling methods exist. In this paper, a discussion is held with respect to different modeling methods. In order to include spatial factors and magnetic nonlinearities, on the one hand, and to restrict the computation time on the other hand, a magnetic equivalent circuit (MEC) modeling method is developed. In order to accelerate numerical convergence, a mesh-based analysis method is applied. The novelty in this paper is the implementation of support vector machine (SVM) to classify the results of simulations at various parameter combinations into successful or unsuccessful synchronization, in order to define the synchronization capability limits. It is explained how these techniques can benefit the simulation time and the evaluation process. The results of the MEC modeling correspond to those obtained with finite element analysis (FEA), despite the reduced computation time. In addition, simulation results obtained with MEC modeling are experimentally validated.

Keywords: LS-PMSM; grid synchronization; MEC modeling; SVM

1. Introduction

In recent years, the interest in high energy-efficient motors is growing, due to increasing energy prices and ecological awareness. Amongst all motors, permanent magnet synchronous motors are developed in order to meet the energy requirements in the IEC 60034-30 standards [1]. For some applications, such as pumps, power start-up circuits are required that can be avoided by adding a squirrel cage in the rotor to accelerate the rotor from standstill [2]. The performance and design of machines is described with different modeling methods in [3–15].

The performance of line start permanent magnet synchronous motors (LS-PMSM) is dependent on design, grid and load parameters. It is essential to have a well-informed idea about the synchronization

capability limits, which is helpful in motor type or design choices. For a fast approach, equivalent schemes in a rotor reference frame (dq) can be used. Based on this approach, software, such as SPEED$^{\circledR}$, has been developed [16]. However, some parasitic effects, such as magnetic saturation, cross-magnetization and differences in rotor bar resistances, are neglected in the transient simulation models [5] and could affect the correct modeling output. To get more reliable and accurate results, numerical techniques like magnetic equivalent circuit (MEC) modeling [7,8,11] and finite elements analysis (FEA) have to be involved. It is also possible to use FEA complementarily with SPEED$^{\circledR}$, in order to correct the equivalent circuit parameters or to calculate iron loss [17]. The magnetic flux in an LS-PMSM depends on the rotor position and the saturation of the ferromagnetic material. The magnetic saturation will cause variations in phase inductances and back-electromotive force (EMF). Such variations of the inductances for interior permanent magnet synchronous machines (IPMSM) can be computed as functions of the line current by means of an FEA model done in preprocessing before simulation in the time domain [18]. On the one hand, FEA will give the most accurate results; on the other hand, changing the design parameters requires a reconstruction of the FEA model [7]. The process takes a long time and is very computationally intensive. A method of interest to meet the compromise between accuracy and speed requirements, MEC can be used, especially in design optimization software [7,8,11,17,19,20]. The computation of an MEC model can be done by two methods [21]. The first method is the node-based analysis that is derived from Kirchhoff's current law (KCL) and used in [7,11], while the other one, namely the mesh-based analysis, is based on Kirchhoff's voltage law (KVL) [19,22]. However, in [8], stator slotting is neglected, and position dependency is not taken into account. In [17,23], a more complex air gap reluctance modeling for IPMSM taking slotting into account is presented. This modeling method is also used to compute the start-up torque in LS-PMSM [7]. To increase the accuracy of the MEC start-up model, the number of flux paths or branches can be increased, subsequently causing a computation time and complexity increase, such that the advantage relative to FEA will be lost [17].

In this paper, a simulation method implemented in the MATLAB$^{\circledR}$ environment is presented in order to be able to study the dynamic behavior of LS-PMSM. The energy conversion is calculated with MEC modeling, such as in [7,19,20]. In contrast to [7], wherein node-based MEC is used to model the LS-PMSM dynamics, here a mesh-based analysis is applied. As in this paper, nonlinear parameters will be used, this method facilitates convergence compared to the node-based analysis [24,25]. In [23], an analytical air gap permeance function is presented to be used in the node-based analysis. In mesh-based analysis, an algorithm that excludes the zero permeances from the air gap permeance/reluctance matrix is essential [22,26], which is called the dynamic management of air gap reluctances in [22]. The contribution in this paper is an algorithm to define the dynamic management of the air gap reluctances based on the aforementioned analytical air gap permeance function.

A magnetic network is developed in which the number of branches is kept low, but still keeping the slotting and saturation into account. To reduce computation time, look-up tables (LUTs) are preprocessed, e.g., position-dependent reluctance matrices. Then, based on these LUTs and simulations in the time domain in Simulink, the dynamic performance is discussed during the synchronization of the LS-PMSM motion with the grid frequency. In this paper an application of this simulation software is exemplified with a study of the effect of lowering the supply voltage, and the vulnerability of the motor stability to this situation is shown. In the first sections hereafter, the MEC model with the different elements will be explained in more detail. Emphasis will be given to the nonlinear and position-dependent reluctances, the dynamic management of the reluctances and the MEC network. These methods are used to discuss the synchronization capability of the LS-PMSM to the grid frequency. In [13,14] the discussion of the synchronization capability is given based on analytical methods. Those analytical methods can be used for a swift parameter evaluation. The drawback is the inaccuracy of these methods [14,15], leading to bad predictions of the applicability. In [15], the authors have used numerical techniques to discuss synchronization with the moment of inertia and cage

design variations. The many repetitive simulations result in a long computation time. The authors of [15] brought many contributions to the modeling strategies. In this paper, the novelty is the use of a support vector machine (SVM) in order to limit the number of repetitive simulations. SVM classifies the simulation data into either sets of machine parameters leading to a successful synchronization or into those parameter settings that could lead in certain conditions to unstable machine behavior after start-up. SVM is a statistical learning algorithm and is widely used for classification purposes [27]. In the next sections, a simulation model in time domain is described, and finally, the MEC modeling is benchmarked against results obtained from Flux2D$^\circledR$ FEA. The simulation results obtained with the MEC model are compared to experimental results.

2. Magnetic Network Algorithm

To study dynamic and steady state characteristics of motors, dq -modeling can be used. On the one hand, these modeling methods have a low computational cost; on the other hand, these methods are not accurate enough because constant machine parameters are assumed. If nonlinear material characteristics are used, saturation can be taken into account by adapting the machine parameters to the magnetic state, but the effect of harmonics is neglected. Simulations with finite element analysis (FEA) are more accurate [15], but still have a high computational burden. MEC modeling can be used in order to avoid this computational cost [7,8,10,11,20,23]. This method is based on reluctance networks, and in analogy with electrical networks having current and voltage supplies, it has flux and magnetomotive force (MMF) sources respectively. The MEC modeling allows one to perform dynamic simulations as done in [10,11,20,23]. In this paper, the MEC model is used to investigate the behavior of line start permanent magnet motors, as in [7,8,11,23]. In [7,11,23], the tooth reluctances are taken into account, while in [8], the reluctance network is reduced to the magnetic paths defined by the direct and quadrature axis and the leakage paths. In [7,8], MEC has been used for rapid design optimization and focuses on the effect of various design parameters on important starting and steady state parameters, more specifically, starting torque and efficiency. In [11,23], MEC has been used in dynamic simulations. In [11], the results are compared with FEA. Often, the MEC results show good agreement with the more accurate FEA results. In MEC, the magnetic flux paths are abstracted to a network of linked flux tubes and can be solved in a similar way as electric circuits are solved. Where two or more flux tubes, or branches, are connected with each other, a node exists. Where two or more branches form a loop, a mesh exists. The MEC can be solved based on the Kirchhoff current law; the fluxes cancel each other in a node. This method is called the node-based method. Another method, mesh-based MEC modeling, is based on the Kirchhoff voltage law. In [7,11,23], a node-based MEC modeling is used. To reach numerical convergence with the node-based MEC model [20,24,25], it takes many iterations, and due to the limit of iterations, the system does not always converge. The implementation of relaxation factors will solve this problem, on the one hand, but on the other hand, this will increase complexity and computational cost [20]. To speed up convergence and to avoid the use of relaxation factors, mesh-based modeling can be used.

The network of an MEC model consists of several nodes with a magnetic potential u. Each node is connected to another node through a branch. Such branches have properties determined by their physical nature. The magnetic circuit of a single branch is presented in [11]. The branch consists of active and/or passive elements, in this paper MMF sources and reluctances, respectively. The active elements can vary as a function of time in the case of alternating current, such as the one flowing through the stator windings, or can be constant in the case of a direct current, a means to model the permanent magnet field. In this paper, MEC-modeling is applied to an LS-PMSM with stator s and rotor r, for which the topology is presented in the cross-section of Figure 1. This motor has N_s stator teeth and N_r rotor teeth. Next to the cross-section, a figure of the MEC model is shown. In this model, the group of passive elements is classified into three subcategories, namely the constant, position-dependent and current-dependent reluctances. This network contains meshes, and in each mesh, a loop with a circulating mesh flux can be defined. By applying KVL, the magnetic networks,

which are comprised if a system of nonlinear algebraic equations, can be developed [24]. In this system with N_l number of meshes, an input vector of mesh MMFs $\mathcal{F}_l^{(N_l \times 1)}$, wherein those which are not related with a source are zero, and a mesh reluctance matrix $\mathbf{A}_R^{(N_l \times N_l)}$, can be defined from which the output mesh flux $\mathbf{\Phi}_l^{(N_l \times 1)}$ can be computed, given by the following matrix equation [20]:

$$\mathbf{A}_R \mathbf{\Phi}_l = \mathcal{F}_l \tag{1}$$

The different types of reluctances that can be found in the reluctance branch vector are discussed hereafter.
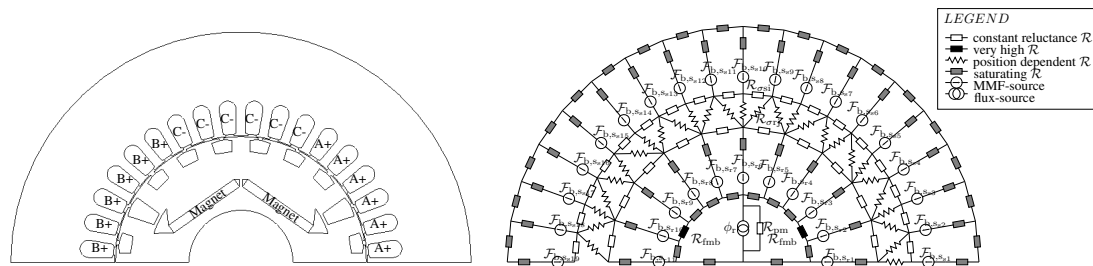

Figure 1. Half cross-section and magnetic equivalent circuit (MEC) model of line start permanent magnet synchronous motors (LS-PMSM).

2.1. Constant Reluctances

In general, a constant reluctance $\mathcal{R}_c$ between two scalar magnetic potentials at location points p_1 and p_2 can be defined as is done in [23]. The distance between those points can be divided into partial distances with each a length dp, an area $A(p)$ and a relative permeability $\mu_r(p)$. The sum of those partial functions leads to:

$$\mathcal{R}_c = \int_{p_1}^{p_2} \frac{1}{\mu_0 \mu_r(p) A(p)} dp \tag{2}$$

Constant reluctances make MEC modeling easier and reduces the computation time, because of a reduction of the number of nonlinear variables. In this point of view, assumptions are made for the MEC model of the LS-PMSM. In Figure 1, the constant reluctances are presented by a white filled resistor symbol. In this paper, leakage reluctances in the stator ($\mathcal{R}_{\sigma s,i}$) and rotor ($\mathcal{R}_{\sigma r,j}$) are assumed to be constant due to the low permeance of air and the long distance of the leakage flux path through the air for the given machine. The values of the leakage reluctances are calculated in the same way as presented in [11], where the total slot leakage reluctance is the equivalent of a parallel circuit of reluctances, calculated with the dimensions of simplified shapes derived from the slot geometry and dependent on the position of the windings.

The reluctance of the magnet ($\mathcal{R}_{PM}$) is also assumed to be a constant in this paper. Neodymium iron boron (NdFeB) magnets are used, for which the relative recoil permeability is assumed to be constant and close to unity. In parallel with this reluctance, there is a reluctance ($\mathcal{R}_{fm}$) that represents a path with ferromagnetic material properties. These paths are called ferromagnetic bridges. Due to the saturation of these bridges, in [6], the reluctance of this path is assumed to be constant, and the permeability is equal to the permeability of a vacuum (μ_0).

The reluctance symbols filled in black are very high constant reluctances and represent the air barriers' reluctances ($\mathcal{R}_{ab}$), the space that obstructs magnet leakage. The distance relative to the area of this reluctance is very high. The parallel circuit of the latter two reluctances give reluctance ($\mathcal{R}_{fmb}$) shown in black in Figure 1.

2.2. Position-Dependent Reluctances

Air Gap Reluctances

In Figure 2, the relation between two teeth is shown in a linear representation of a circular geometry, with a rotor tooth below in the figure, and the tooth above presents a stator tooth. The rotor tooth has a rotor tooth width w_{rt} and a rotor slot opening width o_{rt}. The stator has a stator tooth width w_{st} and a stator slot opening width o_{st}. The stator tooth pitch τ_s is the angle taken from one side of the stator tooth to the other side of that tooth, and with r_{stat} the inner radius of the stator $\tau_s = \frac{w_{st}}{r_{stat}}$. Depending on the rotor position, a tooth will be connected or not connected. The rotor tooth starts to overlap a stator tooth from the moment the center line of the rotor slot opening corresponds to the center line of the stator slot opening (Figure 2a). After a rotation with angle $\frac{\tau_s + \tau_r}{2}$, the center line of the stator tooth is aligned with the center line of the rotor tooth as in Figure 2b. After an angular displacement $\frac{\tau_s + \tau_r}{2}$, the overlap is over and the connection, as well.
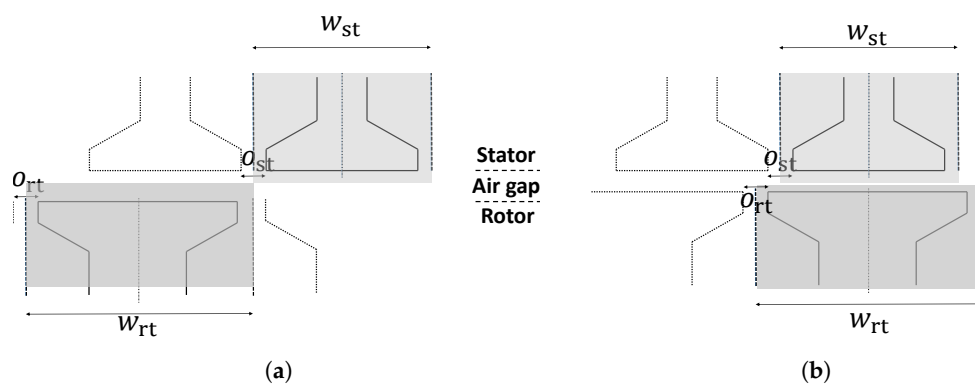

(**a**)   (**b**)

Figure 2. Tooth overlap at different positions: start/end of the overlap (**a**) and completely aligned (**b**).

In the air gap, with air gap length g, connections between a stator tooth i in node $p_{s,i}$ and a rotor tooth j in node $p_{r,j}$ can be presented by flux tubes with a certain air gap permeance $\Lambda_{agi,j}$. These connections are represented with a zigzag drawn element in Figure 1. A close up of the reluctance network between stator teeth and rotor teeth is given in Figure 3, with air gap reluctance values:

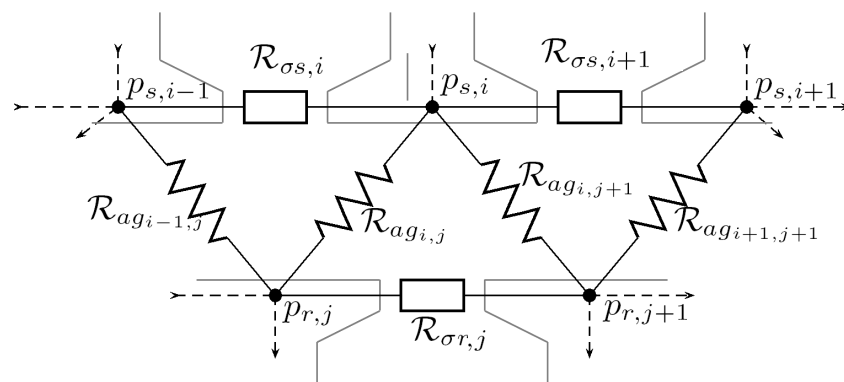$$\mathcal{R}_{agi,j} = \frac{1}{\Lambda_{agi,j}} \tag{3}$$

Figure 3. Reluctance network between the stator and rotor teeth.

The permeance varies as a function of the position θ; with θ_{ref} the reference position. This is the position where the center line of Stator Tooth 1 lays in the direction of the center line of Rotor Tooth 1,

and θ_m is the mechanical position, in a counter clockwise direction, or the displacement relative to θ_{ref} and τ_s the stator tooth pitch and τ_r the rotor tooth pitch. The position is given by:

$$\theta = \theta_m + (\tau_r \cdot (j-1) - \tau_s \cdot (i-1)) \tag{4}$$

An analytical approximation of the permeance function is described in [23]. The overlap between stator tooth i and rotor tooth j is maximum if the teeth are aligned and zero if the teeth are misaligned. The maximum air gap permeance, which corresponds with the aligned position, is determined by the minimum tooth width. For the motor geometry in this paper (Figure 1), this minimum tooth width is the stator tooth width w_{st} and is less than the rotor tooth width w_{rt}.

$$w_{min} = \min(w_{st}, w_{rt}) \tag{5}$$

with L_{stk} the stack length; the maximum permeance is:

$$\Lambda_{ag,max} = \mu_0 \frac{L_{stk} w_{min}}{g} \tag{6}$$

As long as there is a total overlap between stator and rotor with radius r_{rot}, this permeance stays the same, as shown in Figure 4a. In this figure, θ is zero at the aligned position. At a certain position θ_t', the overlap starts to decrease until there is no overlap at rotational displacement θ_t. With stator slot opening o_{ss} and rotor slot o_{sr}, the values of these positions are [10,23]:

$$\theta_t' = \frac{\frac{|w_{st} - w_{rt}|}{2}}{r_{rot} + \frac{g}{2}} \tag{7}$$

$$\theta_t = \frac{\frac{w_{st} + w_{rt} + o_{ss} + o_{sr}}{2}}{r_{rot} + \frac{g}{2}} \tag{8}$$

The air gap permeance function, which is due to the symmetry given in the interval $[-\pi, \pi]$ and shown in Figure 4a, can be defined as:

$$\Lambda_{ag\,i,j} = \begin{cases} \Lambda_{ag,max} & |\theta| \leq \theta_t' \\ \Lambda_{ag,max} \frac{1+\cos\left(\pi \frac{|\theta|-\theta_t'}{\theta_t-\theta_t'}\right)}{2} & \theta_t' \leq |\theta| \leq \theta_t \\ 0 & \theta_t \leq |\theta| \leq \pi \end{cases} \tag{9}$$

While in node-based methods, it is possible to connect the magnetic potential of each stator tooth to every potential of each rotor tooth, it is not possible to connect every tooth, in mesh-based models [22], and hence, a configuration of $N_s \times N_r$ branches cannot be established. This demands an algorithmic management of the air gap reluctance branches. Nevertheless, due to the fact that the number of air gap reluctance branches can be reduced to $N_s + N_r$ branches, convergence is reached faster in the case of nonlinear problem solving. This results in a mesh-based model air gap reluctance matrix $\mathcal{R}_{b_{ag}}^{((N_s+N_r)\times 1)}$ with elements $\mathcal{R}_{b_{ag},i}$.
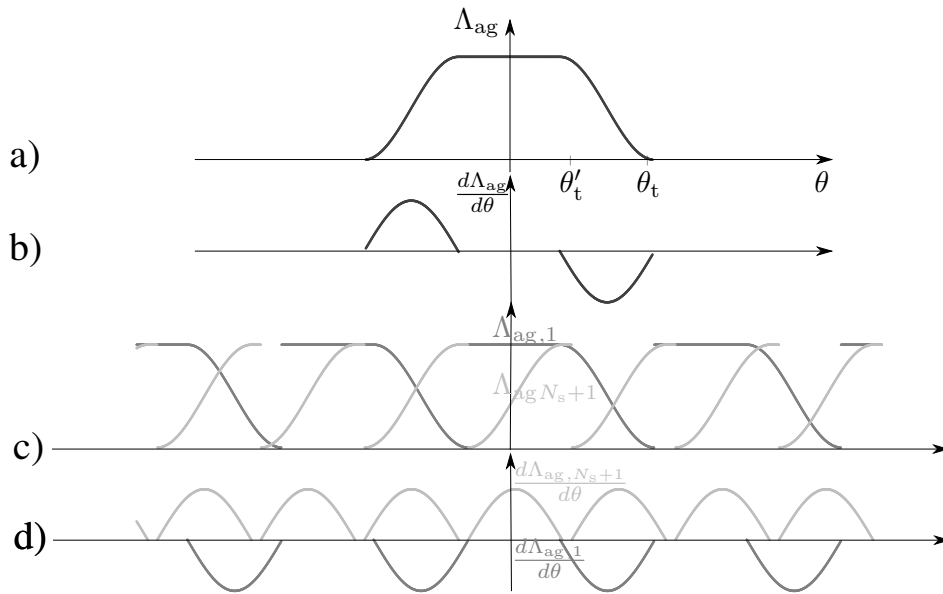
Figure 4. (**a**) Position-dependent air gap permeance function for one stator tooth to rotor tooth connection; (**b**) derivative of the position-dependent air gap permeance function for one tooth-to-tooth connection; (**c**) air gap permeance function in the stator tooth reference (dark gray) and rotor tooth reference (light gray); (**d**) derivative of the air gap permeance function in the stator tooth reference (dark gray) and rotor tooth reference (light gray).

In this matrix $\mathcal{R}_{\mathrm{b_{ag}}}$, there are N_s branches that have a fixed connection with the stator teeth, and N_r branches of $\mathcal{R}_{\mathrm{b_{ag}}}$ are always fixed to the rotor teeth. The branch reluctance vector is from Element Number 1 to N_s filled with reluctances i that are constantly connected to their respective stator tooth nodes i. From position N_s+1 to $N_s + N_r$, this vector is filled with reluctances $N_s + j$ that are constantly connected to their respective rotor tooth nodes j. Each branch is part of two meshes. The branches keep being part of one mesh, and the other mesh is variable along the position θ_m. In Figure 5, the branches that correspond with stator tooth i are marked in dark gray, while the branches that correspond to rotor tooth number j are marked in light gray. In Figure 4d, the partition in the position-dependent permeance function is shown in the same colors.
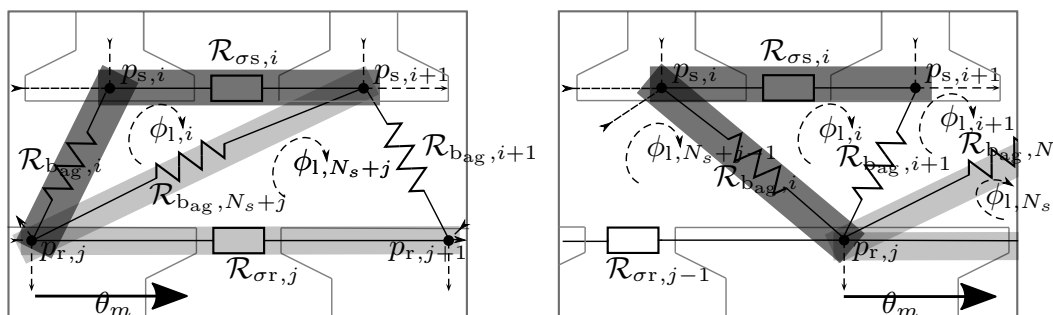

Figure 5. Position dependency of air gap branch reluctances and mesh flux.

This function is divided in two parts, namely $\Lambda_{\mathrm{ags}i,j}(\theta_{\mathrm{m}})$ and $\Lambda_{\mathrm{agr}i,j}(\theta_{\mathrm{m}})$, given by:

$$\Lambda_{\mathrm{ag}i,j}(\theta_{\mathrm{m}}) = \Lambda_{\mathrm{ags}i,j}(\theta_{\mathrm{m}}) + \Lambda_{\mathrm{agr}i,j}(\theta_{\mathrm{m}}) \tag{10}$$

The first permeance function is always part of the air gap mesh $x = i$, and the other one is always part of air gap mesh $y = j + N_\text{s}$. The sum of all permeance functions of stator tooth i including all rotor tooth connections is given by:

$$\Lambda_{\text{b}_{\text{ag}},i}(\theta_\text{m}) = \sum_{j=1}^{N_\text{r}} \Lambda_{\text{ag}_\text{s}i,j}(\theta_\text{m}) \tag{11}$$

In Figure 4c, it is shown in black solid and dotted lines, while the sum of all permeance functions of stator tooth j including all stator tooth connections is given by:

$$\Lambda_{\text{b}_{\text{ag}},N_\text{s}+j}(\theta_\text{m}) = \sum_{i=1}^{N_\text{s}} \Lambda_{\text{ag}_\text{r}i,j}(\theta_\text{m}) \tag{12}$$

This equation is shown in gray solid and dotted lines in Figure 4c. The elements $\Lambda_{\text{b}_{\text{ag}},i}$ can be listed in an air gap permeance vector ($\mathbf{\Lambda}_{\text{b}_{\text{ag}}}^{((N_\text{s}+N_\text{r})\times 1)}(\theta_\text{m})$). At the first moment, the rotor tooth with node j starts to connect with node $i + 1$. This connection has reluctance $\mathcal{R}_{\text{b}_{\text{ag}},N_\text{s}+j}$. Node $p_{\text{s},i+1}$ still has connection with node $j + 1$. At the moment the slot opening at the right side of the stator tooth with node $i + 1$ overlaps the slot opening at the right side of rotor tooth with node j totally, this rotor tooth detects the stator tooth with node $i + 2$ and starts to make a connection with reluctance $N_s + j$. At that moment, also the connection between $i + 1$ and $i + 1$ is disrupted, and the reluctance $\mathcal{R}_{\text{b}_{\text{ag}},i+1}$ can be used to maintain the connection between $i + 1$ and j.

At that moment, also the variable mesh of $i + 1$ changes number from $N_\text{s} + j$ to i. This phenomenon repeats continuously, with the period equal to the stator tooth pitch τ_s, as the rotor rotates. In Figure 6, we can follow the evolution of the inverse of $N_\text{s}+1$, namely $N_\text{s}+1$. Furthermore, we can see that the variable mesh number increments with the falling edge of the permeance pulses, with period equal to the rotor tooth pitch τ_r, until it is reset by a total revolution.
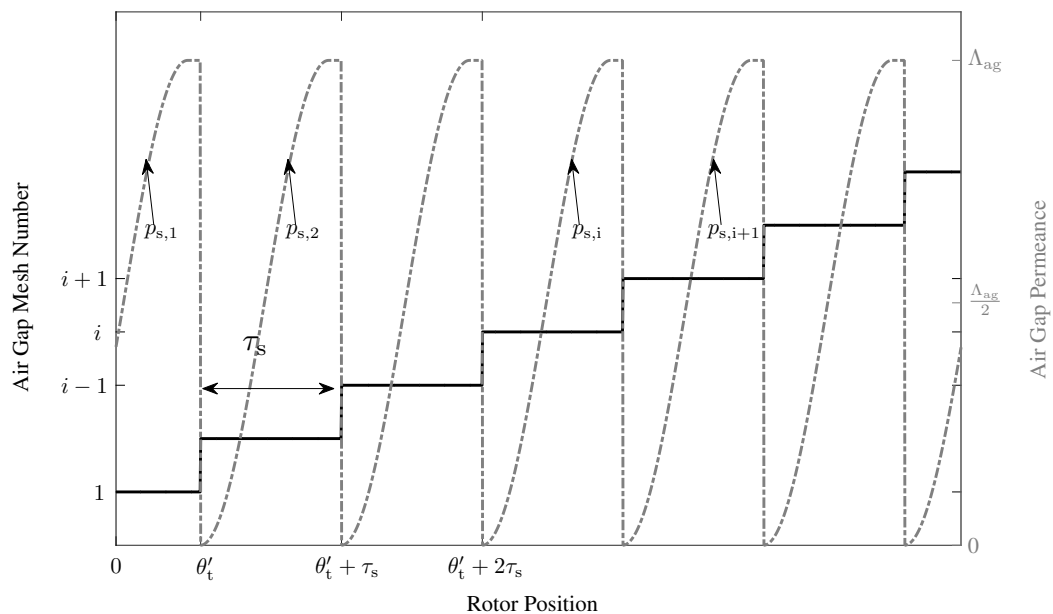

Figure 6. Air gap mesh number (left vertical axes) seen by a branch constantly linked to a rotor tooth $j = 1$ with a pulsating air gap permeance (right vertical axes).

In Figure 7, we can follow the evolution of the inverse of 1, namely 1. Furthermore, we can see that the variable mesh decrements with the rising edge of the permeance pulse of the next tooth that the rotor sees, namely tooth N_s; if the edge of the concerning tooth (Tooth 1) rises, the variable mesh number is equal to the number of the next overlapping tooth (tooth N_s).
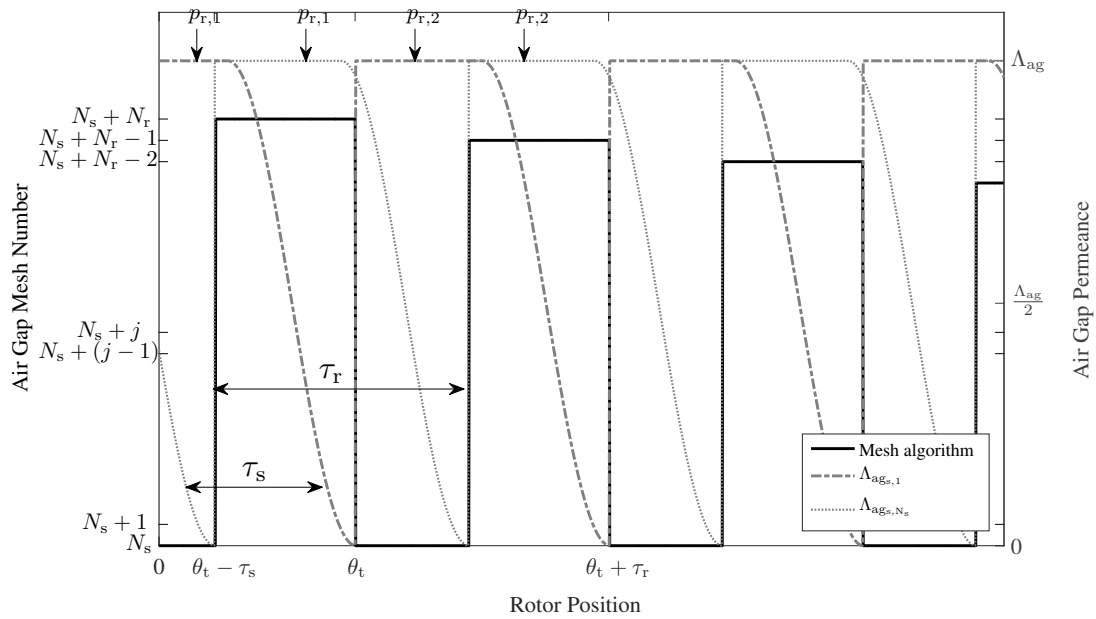
Figure 7. Air gap mesh number (left vertical axes) seen by a branch constantly linked to a stator tooth $i = 1$ with a pulsating air gap permeance (right vertical axes).

2.3. Nonlinear Reluctances

Ferromagnetic materials have nonlinear curve characteristics. In this paper, it is assumed that the curves are anhysteretic. These anhysteretic curves present the relationship between the flux density B and the field intensity H. The relation depends on the material properties. For mesh-based algorithms where the MEC is formulated in terms of mesh equations Equation (1), the permeability is formulated as a function of permeability:

$$B = \mu_{\text{B}}(B)H \tag{13}$$

In a mesh-based approach, each nonlinear reluctance $\mathcal{R}_{\text{b}_{\text{nl}},i}$ with area $A_{\text{b}_{\text{nl}},i}$ and length $l_{\text{b}_{\text{nl}},i}$ is dependent on flux through the reluctance branch $\phi_{\text{b}_{\text{nl}},i}$ [21]:

$$\mathcal{R}_{\text{b}_{\text{nl}},i}(\phi_{\text{b}_{\text{nl}},i}) = \frac{l_{\text{b}_{\text{nl}},i}}{A_{\text{b}_{\text{nl}},i}\mu_{\text{B}}\left(\frac{\phi_{\text{b}_{\text{nl}},i}}{A_{\text{b}_{\text{nl}},i}}\right)} \tag{14}$$

Al these reluctances with a magnetic flux density-dependent permeability create a nonlinear set of equations.

2.4. Active Elements

2.4.1. Magnet MMF Source

The permanent magnets in the rotor ensure a nonzero magnetic field. In a magnetic circuit, this can be modeled as flux sources [4]. Initially, the flux Φ_{r} is dependent on the remanent induction B_r of the magnets. This source flux feeds the leakage flux reluctance $\mathcal{R}_{\text{fmb}}$. With h_{m} the magnet thickness, the MMF source $\mathcal{F}_{\text{M}}$ can be calculated as:

$$\mathcal{F}_{\text{M}} = -h_{\text{m}}H_{\text{c}} \tag{15}$$

The Thevenin equivalent MMF $\mathcal{F}_{\text{Th}}$ of the flux source is:

$$
\begin{aligned}
\mathcal{F}_{\text{Th}} &= \mathcal{R}_{\text{fmb}}\Phi_{\text{r}} \\
&= \mathcal{R}_{\text{fmb}}\frac{-h_{\text{m}}H_{\text{c}}}{\mathcal{R}_{\text{PM}}}
\end{aligned}
\tag{16}
$$

2.4.2. Stator and Rotor MMF

The stator current through each phase is expressed by $\mathbf{i}_{\text{ph}}^{(N_{ph}\times 1)}$. These stator currents can be transformed to stator tooth MMF ($\mathcal{F}_{\text{st}}^{(N_{\text{s}}\times 1)}$) with a winding transformation matrix w'':

$$
\mathcal{F}_{\text{st}} = \mathbf{w}''\mathbf{i}_{\text{ph}}
\tag{17}
$$

Most LS-PMSM have a squirrel cage. The electric circuit of a squirrel cage can be presented by a chain of frames [23], as presented in Figure 8. Each frame has one leg in common, namely a rotor bar, and a segment of the end rings at each side (top and bottom in the figure). Through each frame, there is one current loop i_{l_j} equal to the rotor tooth MMF ($\mathcal{F}_{\text{rt}_j}$). Because the chain is closed, there is also a loop current through the end windings i_{e}. In the figure, the direction of the tooth flux ϕ_{rt_k} of each tooth k is shown.
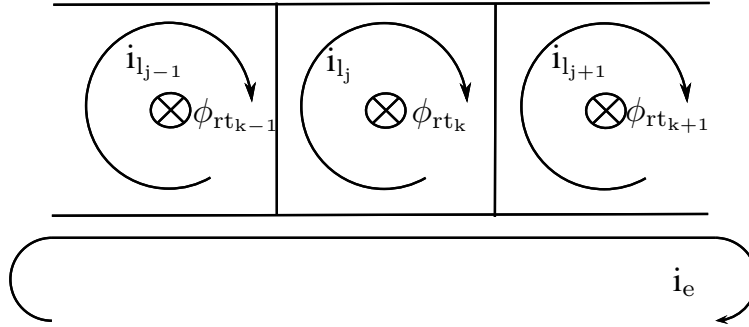

Figure 8. Current loops in a rotor cage.

The values of these sources are listed in a branch source MMF vector $\mathcal{F}_{\text{bs}}^{(n_{\text{b}}\times 1)}$.

2.5. MEC Network

All reluctances are listed in a branch reluctance vector $\mathcal{R}_{\text{b}}^{(N_{\text{b}}\times 1)}$. In the mesh formulation Equation (1), $\mathcal{R}_{\text{b}}$ has to be substituted in a mesh reluctance matrix $\mathbf{A}_{\text{R}}^{(N_{\text{l}}\times N_{\text{l}})}$ by a mesh analysis formulation algorithm (MAFA) [21] and will be described hereafter. This algorithm has n_{b} iterations until all branch reluctances are substituted into $\mathbf{A}_{\text{R}}$. This mesh reluctance matrix $\mathbf{A}_{\text{R}}$ is first initialized as a zero matrix [26]. Each reluctance of branch i is member of a maximum two meshes, x and y. With the formulation in Equation (22), all elements of the mesh reluctance matrix can be calculated.

$$
\begin{aligned}
\mathbf{A}_{\text{R}_{x,x}} &= \mathbf{A}_{\text{R}_{x,x}} + \mathcal{R}_{\text{b},i} \\
\mathbf{A}_{\text{R}_{y,y}} &= \mathbf{A}_{\text{R}_{y,y}} + \mathcal{R}_{\text{b},i} \\
\mathbf{A}_{\text{R}_{x,y}} &= \mathbf{A}_{\text{R}_{x,y}} - \mathcal{R}_{\text{b},i} \\
\mathbf{A}_{\text{R}_{y,x}} &= \mathbf{A}_{\text{R}_{y,x}} - \mathcal{R}_{\text{b},i}
\end{aligned}
\tag{18}
$$

For the branch source vector $\mathcal{F}_{\text{bs}}^{(N_{\text{b}}\times 1)}$, all sources are determined by the equation described in Equation (19), where $s_x = -1$ if the mesh flux $\phi_{\text{l},x}$ of mesh xhas the same direction as the branch flux $\phi_{\text{b},i}$ of branch i and $s_x = 1$ if the mesh flux is reverse to the direction of to branch flux [21]. In this way, $\mathcal{F}_{\text{l}}^{(N_{\text{l}}\times 1)}$ is formulated as:

$$
\mathcal{F}_{\text{l},x} = \mathcal{F}_{\text{l},x} + s_x\mathcal{F}_{\text{b},i}
\tag{19}
$$

To compute the flux in each branch i, in the case of two meshes, the sum of the flux in meshes x and y, $\phi_{l,x}$ and $\phi_{l,y}$, respectively, with s_x and s_y, including that branch, is taken:

$$\phi_{b,i} = s_x \phi_{l,x} + s_y \phi_{l,y} \tag{20}$$

The mesh reluctance matrix $\mathbf{A}_R$ contains nonlinear reluctances. In order to solve the nonlinear system, the Newton–Raphson (NR) method is applied, as explained in [21,25]. The Newton–Raphson method is a numerical method in which the solution converges in iterative steps to a good approximation of the roots of a function. In this method, at each iteration step k, the next estimate $k+1$ is calculated, with $\mathbf{J}$ the Jacobian matrix [25],

$$\begin{aligned} \mathbf{J} &= \frac{\partial(\mathbf{A}_R \mathbf{\Phi}_l)}{\partial \mathbf{\Phi}_l} \\ &= \mathbf{A}_R + \mathbf{D}_R \end{aligned} \tag{21}$$

and the partial derivative terms are given by matrix $\mathbf{D}_R$,

$$\begin{aligned} \mathbf{D}_{R_{x,x}} &= \mathbf{D}_{R_{x,x}} + \frac{\partial \mathcal{R}_{b,i}}{\partial \phi_{l,x}}(\phi_{b,i}) \\ \mathbf{D}_{R_{y,y}} &= \mathbf{D}_{R_{y,y}} + \frac{\partial \mathcal{R}_{b,i}}{\partial \phi_{l,y}}(\phi_{b,i}) \\ \mathbf{D}_{R_{x,y}} &= \mathbf{D}_{R_{x,y}} - \frac{\partial \mathcal{R}_{b,i}}{\partial \phi_{l,x}}(\phi_{b,i}) \\ \mathbf{D}_{R_{y,x}} &= \mathbf{D}_{R_{y,x}} - \frac{\partial \mathcal{R}_{b,i}}{\partial \phi_{l,y}}(\phi_{b,i}) \end{aligned} \tag{22}$$

The next estimation of the mesh flux vector is calculated as:

$$\mathbf{\Phi}_l[k+1] = \mathbf{\Phi}_l[k] - (\mathbf{J}[k])^{-1}\left(\mathbf{A}_R[k]\mathbf{\Phi}_l[k] - \mathcal{F}_l\right) \tag{23}$$

The difference between the next and the present estimate translates to an error metric e defined by the relative precision K_r and the absolute precision K_a [21]:

$$e = \|\mathbf{\Phi}_l[k+1] - \mathbf{\Phi}_l[k]\|_2 - K_r\|\mathbf{\Phi}_l[k+1] + \mathbf{\Phi}_l[k]\|_2 - K_a \tag{24}$$

From the moment e becomes negative, a sufficient approximation of the solution is found.

The conversion from currents to MMF sources in MEC is explained in Section 2.4. In the MEC algorithm, the flux in each branch of the network is computed from the rotor position and the MMF sources. With N_{ph} number of phases, the tooth flux vector ($\mathbf{\Phi}_t^{(N_s \times 1)}$) and transformation matrix ($\mathbf{w}'^{(N_{ph} \times N_s)}$), the flux in rotor and stator tooth branches, calculated by Equation (20), is then converted to a stator and rotor winding formulation by:

$$\mathbf{\Psi} = \mathbf{w}'\mathbf{\Phi}_t \tag{25}$$

The back EMF amplitude of the voltage equation is obtained by the time derivative of this flux.

3. Analysis of an LS-PMSM by Using MEC-Based Time Simulations

An LS-PMSM has a squirrel cage rotor to help start the motor by generating an asynchronous torque, similar to the electromagnetic torque generated in an induction motor. Once the motor is synchronized to the utility grid, the asynchronous torque is zeroed, and the LS-PMSM behaves like a permanent magnet synchronous machine. During start-up, the contribution of the permanent magnet torque has a braking torque effect on average [4]. In addition, the saliency of the motor causes a saliency braking torque. During the synchronization phase of the motor, the sum of all the aforementioned torque components reflected in the pull-in torque could be too low compared to the load torque, hence causing the motor to fail to reach the synchronization phase. Reasons can be found in a critical load-inertia combination as described in [4]. When the synchronization to the

utility grid fails, rotor speed will fluctuate strongly, triggering the rotor cage and therefore heating up the rotor to higher temperatures than expected. It goes without saying that the wanted operation point is a constant synchronous speed, and for this, well-founded knowledge of the synchronization capability is of great importance. As good design parameters as well as external parameters, e.g., load and supply parameters have an effect on the synchronization process. In this paper, the external parameters are discussed. More specifically, the influence of the supply voltage, the load torque and inertia is investigated.

3.1. Dynamical Model of the LS-PMSM

In order to incorporate the dynamical behavior of the machine into the model, a formulation of the electromagnetic torque (T_{em}) has to be determined [20]. In this paper, the torque T_{em} is derived from the field energy function [20,23,26]. With element k of the position-dependent air gap permeance branch vector ($\mathbf{\Lambda}_{b_{ag}}(\theta_m)$), the instant torque of a machine with N_p pole pairs can be calculated:

$$T_{em}(\theta_m, \mathcal{F}_{b_{ag}}) = \left(\frac{N_p}{2}\right) \sum_{k=1}^{(N_s+N_r)} \mathcal{F}_{b_{ag},k}{}^2 \frac{d\mathbf{\Lambda}_{b_{ag},k}(\theta_m)}{d\theta_m} \tag{26}$$

To study the transient performance of an LS-PMSM, with $\mathbf{V}_{sr}{}^{((N_{ph}+N_r)\times 1)}$ the voltage matrix including stator and rotor voltages, $\mathbf{I}_{sr}{}^{((N_{ph}+N_r)\times 1)}$ the current matrix, $\mathbf{R}_{sr}{}^{((N_{ph}+N_r)\times 1)}$ the resistance matrix and $\mathbf{\Psi}_{sr}{}^{((N_{ph}+N_r)\times 1)}$ the flux matrix, the voltage equation is given:

$$\mathbf{V}_{sr} = \mathbf{R}_{sr}\mathbf{I}_{sr} + \frac{d\mathbf{\Psi}_{sr}}{dt} \tag{27}$$

The load equation is a second order equation:

$$T_{em} - T_{load} = T_{loss} + J\frac{d^2\theta_m}{dt^2} \tag{28}$$

By substituting Equation (26) into Equation (28) at each time step, the mechanical position θ_m can be found. The mechanical friction with friction factor ρ_w is assumed to be proportional to the mechanical speed (ω_m), resulting in a friction torque ($T_{loss} = T_w = \rho_w\omega_m$).

Inertia J is the sum of the motor inertia (J_m) and the inertia of the coupled system (J_{sys}):

$$J = J_m + J_{sys} \tag{29}$$

In the flowchart of Figure 9, showing the solving procedure of the magnetic field equations with NR as given in Section 2.5, the inputs are the stator phase currents, rotor bar currents and the rotor position. The outputs are the electromagnetic torque, calculated by Equation (26), and the phase flux, calculated by Equation (25). The position determines the position-dependent reluctance, the mesh list and the position derivative of the permeance obtained from an LUT. From these values, the branch MMF-source vector and the branch reluctance vector follow. The branch vectors will be converted to mesh vectors, and by using NR to solve the nonlinear equation, a solution can be found.

For the simulations based on the mechanical and the electrical equations, in this paper, MATLAB® Simulink R2015b (The MathWorks, Inc., Natick, MA, USA) is used. To solve the differential Equations (27) and (28) in a discrete time step, the Euler method is used. Each time iteration, the nonlinear magnetic field equation is solved with the NR-method. In this method, the rotor position θ_m and rotor/stator current are input. To reduce the number of NR iterations, the branch flux vector from the last time step has been set as the initial state for the NR algorithm in the next time step. The block diagram to model and simulate the dynamical behavior of the LS-PMSM is shown in Figure 10.
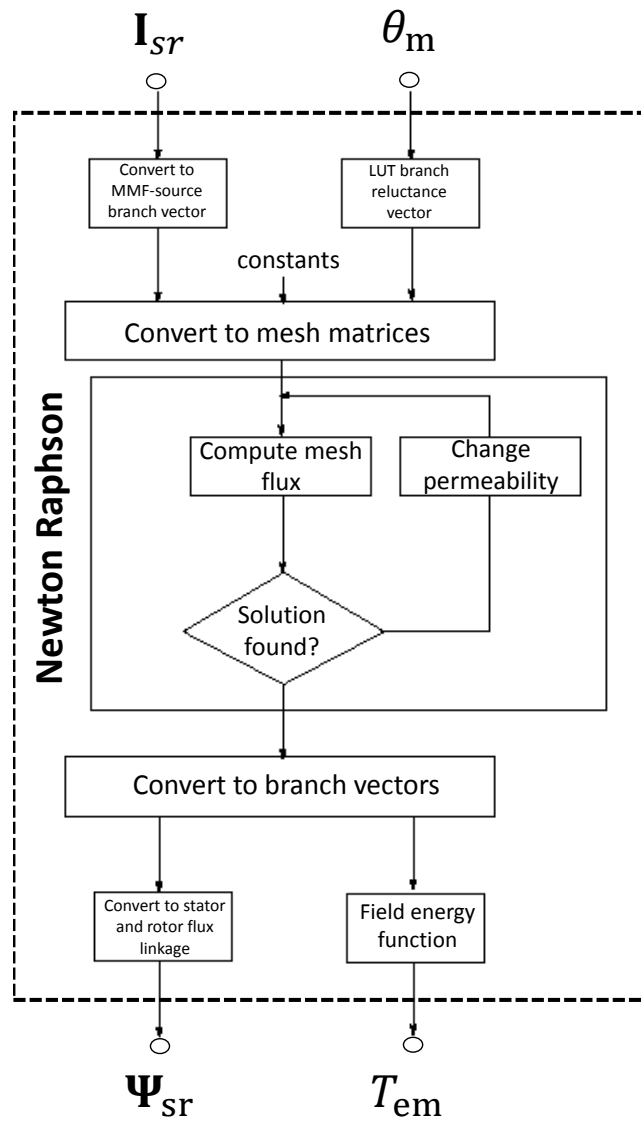
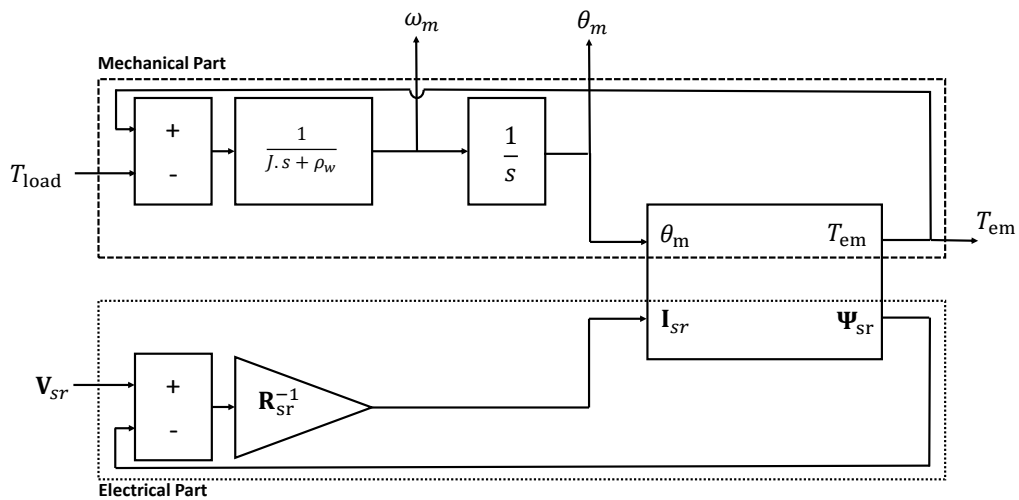**Figure 9.** Flowchart of the MEC algorithm.

Figure 10. Block diagram for the simulation of motor dynamics.

3.2. Synchronization Capability

The analysis of the dynamical behavior of the motor is important for the definition of the synchronization capability limits and allows one to discuss the applicability of this motor in a (pump) system. Of importance is the synchronization capability of the motor with the utility grid. In [13,14], the synchronization capability of LS-PMSM is discussed by using analytical methods. Another issue is the start-up time. A lower time span results in smoother starting. Determining the synchronization with an analytical formula, as done in [14], results in a fast evaluation. These analytical models neglect nonlinearities, and the result shows rather the trends of the synchronization process, but fail in accurately predicting the synchronization capability limits in order to avoid synchronization problems [15]. For this reason, numerical methods are used to define these limits of synchronization capability. The synchronization takes place at the moment the load angle δ, the phase shift between the EMF and the supply voltage, nears the settle point δ_0, namely the steady state load angle, as shown in Figure 11.
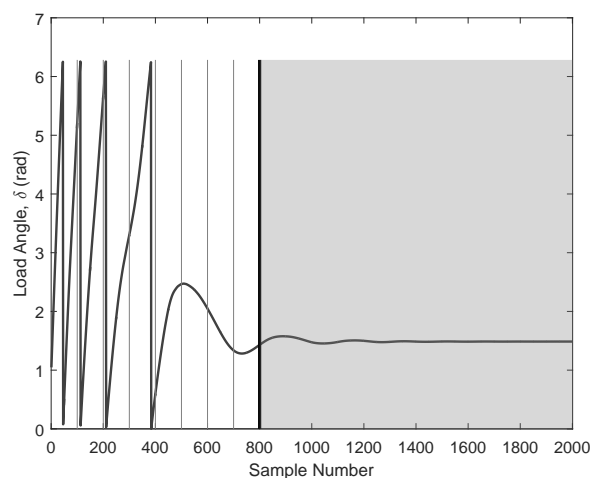

Figure 11. Load angle of a successful synchronization and simulation stop from the moment the synchronization is nearly reached.

The classification, whether or not stable operation is successfully reached, is defined in this paper by the standard deviation of N discrete time samples for succeeding time spans with duration Δt. Synchronization is reached if it is lower than the boundary ϵ:

$$\sqrt{\frac{1}{N-1}\sum_{k=1}^{N}(\delta(k)-\delta_0)^2} < \epsilon \tag{30}$$

This algorithm to classify the synchronization capability is also used to define the starting up time needed to run from standstill to synchronization. In Figure 12, the synchronization has been studied for three different voltage amplitudes going from 75% over 85% to 90% of the rated voltage. In this figure, it is shown that at 75%, the motor already fails to synchronize at high slip values, hence, low rotor speed values, while the motor synchronizes at 85% of the nominal voltage, but at 90%, the motor goes much faster to synchronization: at 58% of the time spent to go into synchronization compared with the situation of 85% of the nominal voltage. Time simulations require much computational time. This computational time can be reduced by this algorithm, by stopping the simulation from the moment the load angle only varies between the error boundaries; see Figure 11.

The synchronization capability has been studied in Figure 13. The effect of dynamical parameters like inertia is shown in synchronization graphs. For each synchronization graph, a 3three-dimensional mapping of the load torque, inertia and the evaluated parameter is obtained by time simulations in the dq-modeling. At each simulation point, a vector is allocated, determining if the motor fails or not

in synchronization, and the boundaries are defined by SVM. SVM is a statistical learning algorithm and is widely used for classification purposes [27]. Before running the SVM algorithm, a number of samples have to be taken. These predictors, based on estimates, in a parameter space, get a binary value. In this paper, the parameters in the parameter space are the inertia (J) and the load torque (T_{load}). SVM defines a gap, or hyperplane, that separates the points to be classified with the maximum margin. Basically, this hyperplane is linear, but also, nonlinear hyperplanes can be implemented, by defining them in terms of a kernel function. Hence, the accuracy of this machine learning method depends on the number and the position of the predictors and the choice of the kernel function. The error margin may be larger, on the one hand, but the reduction in computational burden is a benefit, on the other hand. Once the hyperplane is accomplished, new simulations with parameters chosen in the margins of the estimated hyperplane, could improve the accuracy. The new operation points denoted with 'Check A' and 'Check B' in Figure 13 prove the functioning of the SVM. It is shown that operation point 'Check A', with no synchronization, is separated by the hyperplane from the operation point 'Check B', with synchronization.
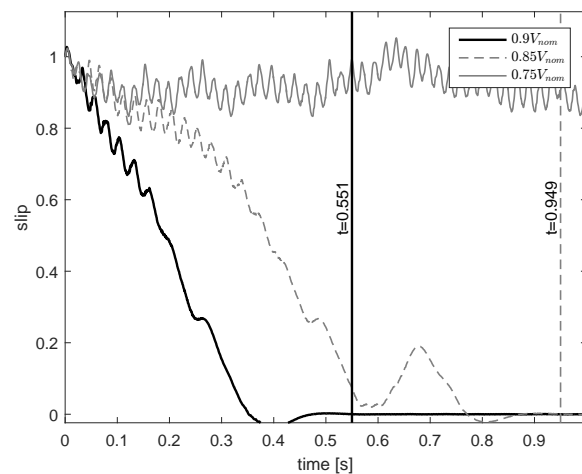

Figure 12. Synchronization capability at voltage variation (inertia of 0.0106 kg·m^2 and nominal torque).
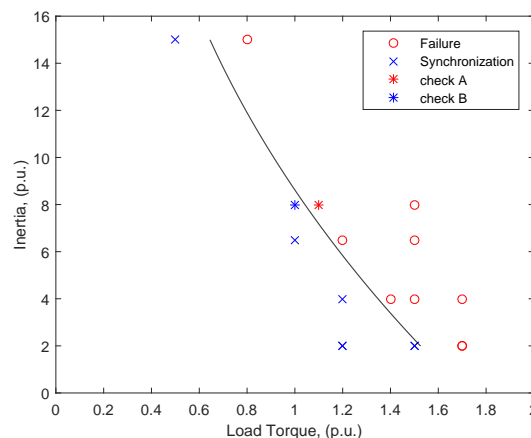

Figure 13. Synchronization capability.

3.3. Results

3.3.1. Simulation Results

The MEC model is evaluated against results obtained with commercial FEA software Flux2D$^{®}$ (Version 10.4, CEDRAT S.A., Meylan Cedex, France).The input parameters for both methods can be

found in Table 1, and the solving process options can be found in Table 2. The computation time has been compared, and the results are given in Table 3. Considering that the number of elements in the FEA method is reduced, but not minimized, the computation time of the MEC computation is 0.38% of the computation time of the FEA computation, which is about 260-times less. In this paper, the simulation program and the MEC model are evaluated step by step. In Figure 14a, one period of the waveform of the electromotive force (EMF) is given at 3000 rpm. In Figure 14b, a fourth of the period has been enlarged. In this figure, the differences between the MEC results and the FEA results are clearer. The harmonic distortion amplitudes of the EMF are higher in the case of FEA. Due to a transitional phenomenon caused by the mesh algorithm in the air gap, there is more numeric noise in the waveforms of the MEC. The harmonic content of the EMF waveform, obtained after a fast Fourier transform (FFT) analysis, is shown in Figure 15. In this figure, the values are given. In Figure 15a, the harmonic content of the FEA simulation is given, while Figure 15b shows the harmonics of MEC. The orders of the harmonics correspond; the magnitude of the fundamental harmonic is almost the same for MEC and FEM. For the higher harmonics, the magnitude is less in most cases. The cogging torque is given in Figure 16. In this figure, the effect of the slotting is much more pronounced in the waveform calculated by FEA simulations compared to the waveform calculated by MEC simulations. In the MEC model, a smooth air gap permeance function is used. This function is only position dependent. In contrast with the FEA model, the saturation in the tooth tips is not implemented in the MEC model.

Table 1. Machine data of a 3-kW 2-pole LS-PMSM.

Symbol	Parameter	Value
V_{nom}	nominal voltage	380 V
P_{nom}	nominal power	3 kW
f_{nom}	nominal frequency	50 Hz
N_{nom}	nominal speed	3000 rpm
T_{nom}	nominal torque	9.55 Nm
J_{m}	motor inertia	0.0053 kg·m^2
N_{ph}	number of phases	3
N_{p}	number of poles	2
N_s	number of stator teeth	36
N_{r}	number of rotor teeth	20
g	air gap length	0.3 mm
L_{stk}	rotor stack length	103 mm
r_{rot}	rotor radius	42.2 mm
w_{PM}	permanent magnet width	27 mm
l_{PM}	permanent magnet length	103 mm
d_{PM}	permanent magnet thickness	3 mm
B_{r}	permanent magnet remanent induction	1.1 T

Table 2. Solving process options.

Setting	Value
Relative precision (K_{r}) for NR	1×10^{-4}
Absolute precision (K_{a}) for NR	1×10^{-6}
Relaxation	no

Table 3. Computation time.

Material Properties	MEC	FEA
linear	0.007 s	1.6 s
nonlinear	0.014 s	3.67 s

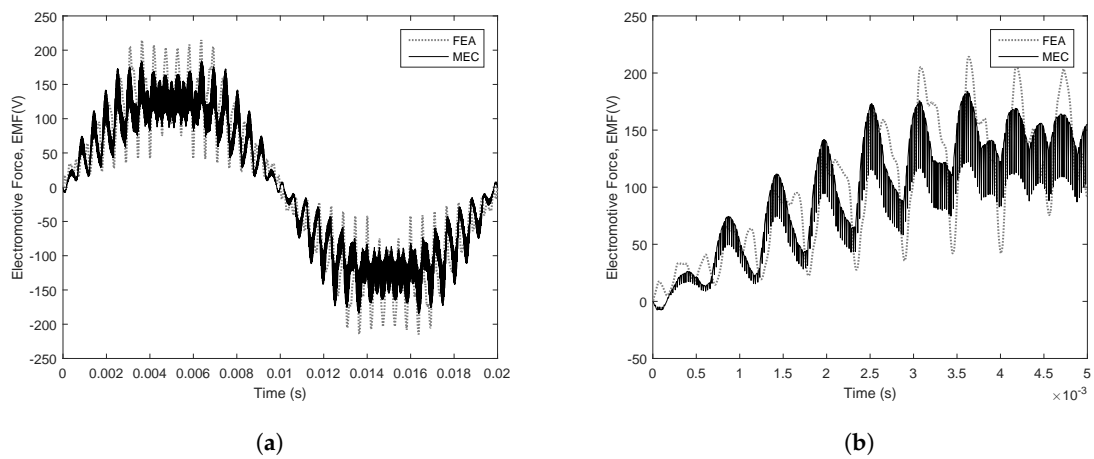**Figure 14.** Electromotive force (EMF) at nominal speed (3000 rpm) for one period in (**a**) and $\frac{1}{4}$ of the period in (**b**); MEC is compared with finite element analysis (FEA).
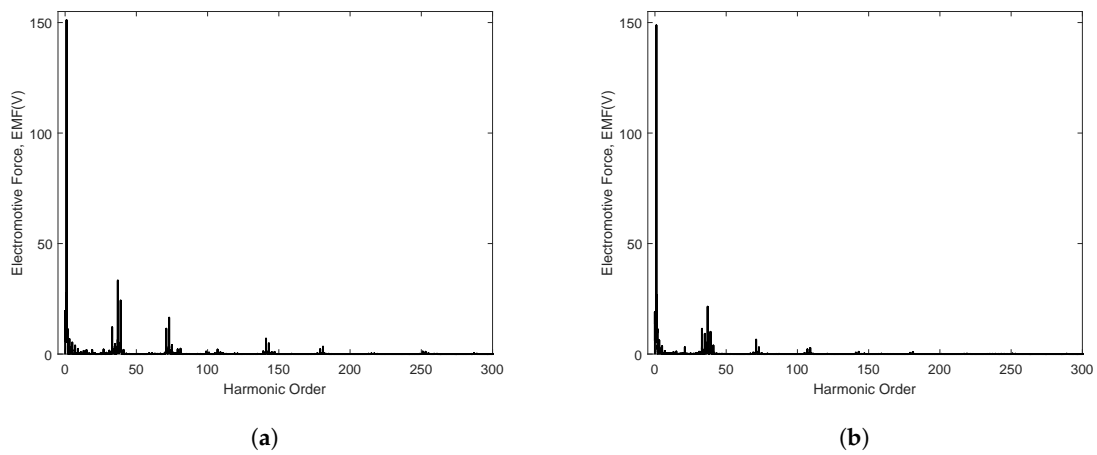

Figure 15. Amplitudes of voltage harmonics of the EMF waveform, as a function of the harmonic order for FEA simulations (**a**) and MEC simulations (**b**).
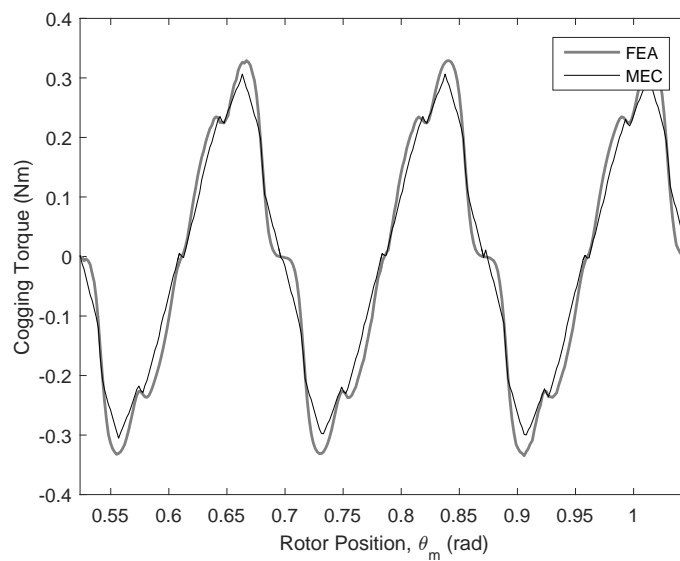

Figure 16. Cogging torque; MEC is compared with FEA.

To research the effect of the stator current on the electromagnetic torque, in Figure 17, a constant stator current of 7 A has been supplied. The rotor has been rotated, and the torque has been calculated. Changing the rotor position results in sinusoidal torque variations due to the salient pole structure and hence a reluctance variation along the air gap. To avoid the influence of the magnets, the spaces provided for the magnets are assumed to be air barriers. The resulting torque is only reluctance torque. Furthermore, the influence of the ferromagnetic material in the stator and rotor has been investigated. In Figure 17a, linear almost infinite permeable, magnetic material is assumed, while in Figure 17b, a simulation with a ferromagnetic nonlinear material is given. Both figures show a good correspondence between FEA and MEC. This does not only show the correspondence between the torque calculation results with only air gap reluctance, but also that there is not much difference between both simulation methods if also the effect of the reluctance of ferromagnetic materials has been included.
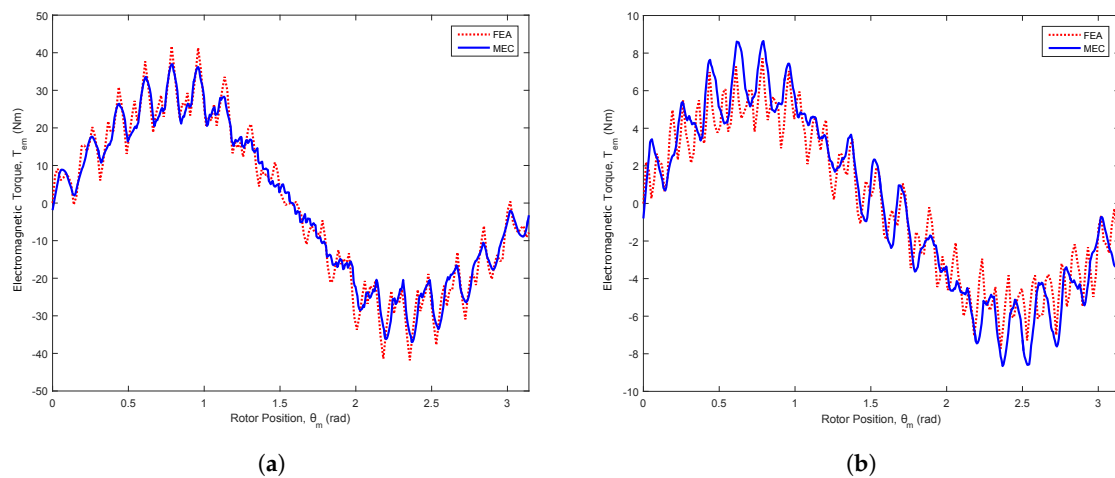

(a)

(b)

Figure 17. Electromagnetic reluctance torque, at 7 A, in the case of (**a**) linear and (**b**) nonlinear magnetical material. There is no influence of permanent magnets. MEC is compared with FEA.

The time step simulation model shown in Figure 10 is programmed in Simulink in order to discuss the synchronization capability of the motor. In the time step simulations of Figure 18, the load torque is set to the nominal torque (9.55 Nm), while the inertia is five-times the motor inertia (0.0265 kg·m^2). The motor goes from standstill to synchronous speed. In these time graphs, only the synchronization process at higher speed values (here from 150 rad/s and higher) is shown. In Figure 18b, the results obtained with MEC simulations are shown, and in Figure 18a, the FEA results are shown. With both simulation models, MEC and FEA, simulations at a supply voltage of respectively 85% and 95% of the nominal voltage are analyzed. With both simulation methods, it is shown that at a voltage of 85% of the nominal voltage, the motor fails to synchronize starting from standstill, while in the case of a voltage of 95% of the nominal voltage, the motor synchronizes with the supply frequency. The simulation results of MEC and FEA show good agreement.
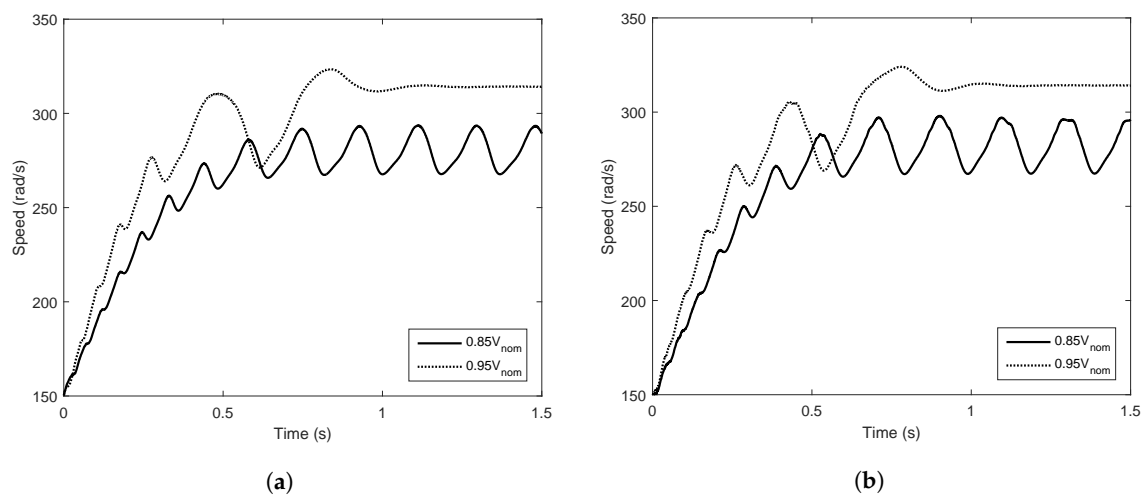
Figure 18. Simulation at nominal torque and five-times the inertia of the rotor, failing in synchronization at 85% of the nominal voltage and succeeding in synchronization at 95% of the nominal voltage, with (**a**) FEA and (**b**) MEC.

3.3.2. Experimental Results

In the simulations of Figure 18, the voltage has been varied in order to discuss synchronization. In the test bench, the LS-PMSM is coupled to a load that is emulated by a permanent magnet (PM) synchronous drive as shown in the schematic overview of Figure 19. The total rotational inertia of this load is 0.0052 kg·m^2 including the couplings, the rotor of the PM machine and the shaft. A power amplifier system (PAS) is used to supply the LS-PMSM. This PAS is remotely controlled by a PC. Voltage waveforms are amplified by differential voltage instrumentation amplifiers included on a printed circuit board (PCB). Speed is measured by a speed encoder. Together with the analog signals from the PCB, this pulse signal is input to the data acquisition (DAQ) system. The torque set value for the drive is programmed in a controlling unit. In the measurements, the torque is kept constant, while the voltage has been varied. The speed is measured and shown in Figure 20 for 324 V (85% of V_{nom}) and 304 V (80% of V_{nom}). These measurements are compared with MEC simulations. From this figure, it follows that there is a good agreement between the measurements and the MEC model-based simulations. The motor in the test setup fails to synchronize at a voltage of 304 V, while the motor synchronizes at 324 V.
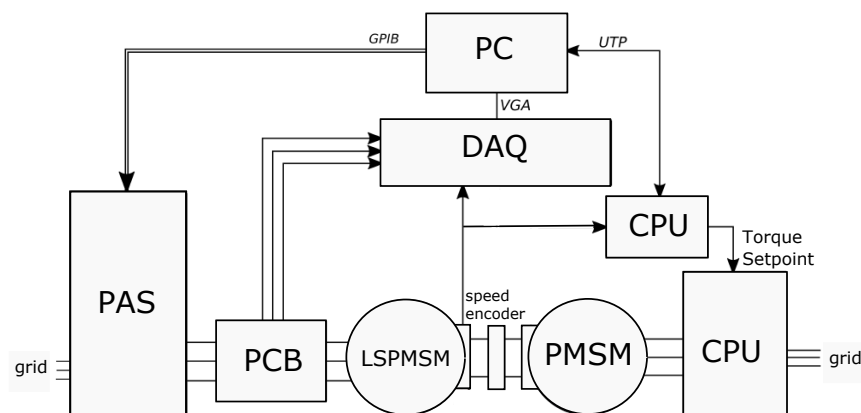

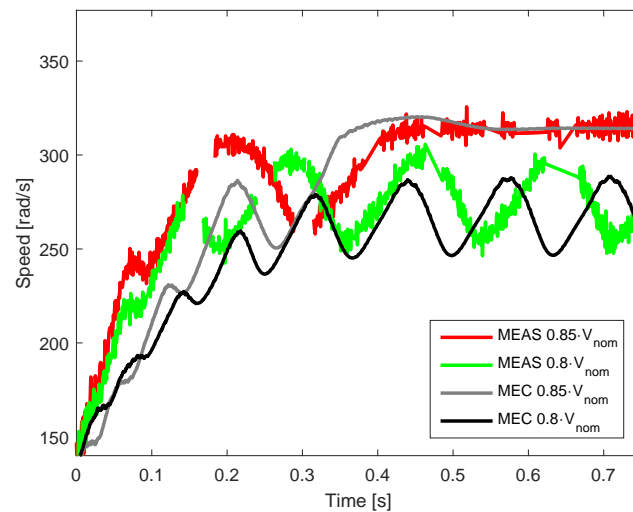**Figure 19.** Schematic overview of the test setup. PAS: power amplifier system.

Figure 20. Effect of the voltage on the synchronization of the motor for a constant torque of 1.5-times the nominal torque, with measurements (MEAS) and MEC simulations.

4. Conclusions

In this paper, a modified dynamic simulation program to study the performance of an LS-PMSM is presented. A comprehensive description of relevant simulation methods is given. The MEC-based time simulations are chosen in order to increase the accuracy compared to dq-based time simulation methods and to reduce computation time compared to FEA-based time. To reduce computation time, many modifications are applied. The computation time can be reduced by reducing the number of Newton–Raphson iterations and the number of elements. The number of elements is reduced by applying simplifications. The number of elements in the network is low, but still taking the slot harmonics into account. Furthermore, the number of elements that have nonlinear material characteristics is reduced if the contribution of their nonlinear properties is rather marginal. The mesh-based algorithm is applied in order to reduce the number of Newton–Raphson iterations. This method does not need relaxation and speeds up the convergence. By feeding the initial states of the iterative process with the results of the previous time step, the number of iterations is reduced. The computation time is compared with the FEA computation time. The MEC simulations are compared with FEA simulations in the static and transient state. The results are given in this paper. With the MEC-based time simulation and the FEA-based time simulation, two operating points are compared in order to discuss synchronization. Time simulations are also validated with experimental test results. These results are convincing to conclude that MEC can be used to replace the slower FEA-based simulation method. The time simulations obtained with the MEC method are analyzed, and a classification of parameter combinations that led to successful or unsuccessful synchronization based on SVM has been computed in order to define the synchronization capability limits. The classification method is validated with additional simulation results from parameter combinations that have been chosen close to the limit.

Author Contributions: All the authors contributed substantially to the work presented. Bart Wymeersch did the programming, simulations and experimental work. In addition, he wrote the paper. Lieven Vandevelde, Frederik De Belie and Claus B. Rasmussen gave advice and revised the manuscript.

References

1. De Almeida, A.T.; Ferreira, F.J.T.E.; Fong, J.A.C. Standards for Super-Premium Efficiency class for electric motors. In Proceedings of the Record 2009 IEEE Industrial Commercial Power Systems Technical Conference, Calgary, AB, Canada, 3–7 May 2009.
2. Miller, T.J.E. Synchronization of Line-Start Permanent-Magnet AC Motors. *IEEE Power Eng. Rev.* **1984**, *PER-4*, 57–58. [CrossRef]
3. Rahman, M.A.; Little, T.A. Dynamic Performance Analysis of Permanet Magnet Synchronous Motors Magnet Synchronous Motors. *IEEE Trans. Power Appar. Syst.* **1984**, *PAS-103*, 1277–1282. [CrossRef]
4. Hendershot, J.R.; Miller, T.J.E. *Design of Brushless Permanent-Magnet Machines*; Motor Design Books LLC: Venice, FL, USA, 2010.
5. Isfahani, A.H.; Vaez-Zadeh, S. Effects of Magnetizing Inductance on Start-Up and Synchronization of Line-Start Permanent-Magnet Synchronous Motors. *IEEE Trans. Magn.* **2011**, *47*, 823–829. [CrossRef]
6. Wymeersch, B.J.; De Belie, F.; Rasmussen, C.B.; Jensen, F.; Vandevelde, L. Influence of ferromagnetic bridges in dq-equivalent-circuit modeling of interior permanent-magnet machines. In Proceedings of the International Conference on Electrical Machines (ICEM), Berlin, Germany, 2–5 September 2014; pp. 1238–1242.
7. Lu, X.; Iyer, K.L.V.; Mukherjee, K.; Kar, N.C. Development of a Novel Magnetic Circuit Model for Design of Premium Efficiency Three-Phase Line Start Permanent Magnet Machines With Improved Starting Performance. *IEEE Trans. Magn.* **2013**, *49*, 3965–3968. [CrossRef]
8. Niazazari, M.; Mirsalim, M.; Mohammadi, S. Analytical framework for analysis and demagnetization study of a slotted solid-rotor line-start permanent-magnet synchronous motor. In Proceedings of the 2014 5th Power Electronics, Drive Systems and Technologies Conference (PEDSTC), Tehran, Iran, 5–6 February 2014; pp. 494–499.
9. Wymeersch, B.; De Belie, F.; Rasmussen, C.B.; Jensen, F.; Vandevelde, L. Mutual-inductance modeling in line-start permanent-magnet synchronous machines based on winding-function theory. In Proceedings of the IEEE International Electric Machines Drives Conference (IEMDC), Chicago, IL, USA, 12–15 May 2013; pp. 607–611.
10. Naderi, P.; Shiri, A. Rotor/Stator Inter-Turn Short Circuit Fault Detection for Saturable Wound-Rotor Induction Machine by Modified Magnetic Equivalent Circuit Approach. *IEEE Trans. Magn.* **2017**, *53*, 1–13. [CrossRef]
11. Takahashi, A. *Dynamic and Steady-State Characteristics of Line-Starting Permanent Magnet Motors (Berichte aus der Elektrotechnik)*; Shaker Verlag GmbH: Herzogenrath, Germany, 2010.
12. Kemmetmüller, W.; Faustner, D.; Kugi, A. Modeling of a Permanent Magnet Synchronous Machine with Internal Magnets Using Magnetic Equivalent Circuits. *IEEE Trans. Magn.* **2014**, *50*, 1–14.
13. Rabbi, S.F.; Rahman, M.A. Critical Criteria for Successful Synchronization of Line-Start IPM Motors. *IEEE J. Emerg. Sel. Top. Power Electron.* **2014**, *2*, 348–358. [CrossRef]
14. Chama, A.; Sorgdrager, A.J.; Wang, R.J. Analytical synchronization analysis of line-start permanent magnet synchronous motors. *Prog. Electromagn. Res. M* **2016**, *48*, 183–193. [CrossRef]
15. Jędryczka, C.; Knypiński, Ł.; Demenko, A.; Sykulski, J.K. Methodology for Cage Shape Optimization of a Permanent Magnet Synchronous Motor Under Line Start Conditions. *IEEE Trans. Magn.* **2018**, *54*, 1–4. [CrossRef]
16. Miller, T.J.E.; McGilp, M.; Wearing, A. Motor design optimisation using SPEED CAD software. In Proceedings of the IEE Seminar Practical Electromagnetic Design Synthesis, London, UK, 11 February 1999; pp. 2/1–2/5.
17. Tariq, A.R.; Nino-Baron, C.E.; Strangas, E.G. Iron and Magnet Losses and Torque Calculation of Interior Permanent Magnet Synchronous Machines Using Magnetic Equivalent Circuit. *IEEE Trans. Magn.* **2010**, *46*, 4073–4080. [CrossRef]
18. De Belie, F.; Melkebeek, J.; Vandevelde, L.; Geldhof, K.; Boel, R. A discrete-time model including cross-saturation for surface permanent-magnet synchronous machines. *Int. J. Comput. Math. Electr. Electron. Eng. (COMPEL)* **2006**, *25*, 766–778. [CrossRef]
19. Bash, M.L.; Williams, J.M.; Pekarek, S.D. Incorporating Motion in Mesh-Based Magnetic Equivalent Circuits. *IEEE Trans. Energy Convers.* **2010**, *25*, 329–338. [CrossRef]

20. Wang, R.; Pekarek, S.; Bash, M.L.; Larson, A.; Maaren, R.V. Incorporating Dynamics in a Mesh-Based Magnetic Equivalent Circuit Model of Synchronous Machines. *IEEE Trans. Energy Convers.* **2015**, *30*, 821–832. [CrossRef]

21. Sudhoff, S.D. *Magnetics and Magnetic Equivalent Circuits*; Wiley-IEEE Press: Hoboken, NJ, USA, 2014.

22. Gyselinck, J.; Sabariego, R. Airgap reluctance identification for the magnetic equivalent circuit modeling of induction machines. In Proceedings of the Conference on the Computation of Electromagnetic Fields (COMPUMAG), Budapest, Hungary, 30 June–4 July 2013; Volume 4, pp. 2820–2827.

23. Ostovic, V. Computation of Saturated Permanent-Magnet AC Motor Performance by Means of Magnetic Circuits. *IEEE Trans. Ind. Appl.* **1987**, *IA-23*, 836–841. [CrossRef]

24. Derbas, H.W.; Williams, J.M.; Koenig, A.C.; Pekarek, S.D. A Comparison of Nodal- and Mesh-Based Magnetic Equivalent Circuit Models. *IEEE Trans. Energy Convers.* **2009**, *24*, 388–396. [CrossRef]

25. Bash, M.; Pekarek, S. Modeling of salient-pole wound-rotor synchronous machines for population-based design. In Proceedings of the 2012 IEEE Power and Energy Society General Meeting, San Diego, CA, USA, 22–26 July 2012.

26. Bash, M.L.; Pekarek, S.D. Modeling of Salient-Pole Wound-Rotor Synchronous Machines for Population-Based Design. *IEEE Trans. Energy Convers.* **2011**, *26*, 381–392. [CrossRef]

27. Liu, G.; Chen, L.; Zhao, W.; Jiang, Y.; Qu, L. Internal Model Control of Permanent Magnet Synchronous Motor Using Support Vector Machine Generalized Inverse. *Trans. Ind. Inform.* **2013**, *9*, 890–898. [CrossRef]